Nanoscale Advances

ROYAL SOCIETY OF CHEMISTRY

PAPER

View Article Online
View Journal | View Issue

Cite this: *Nanoscale Adv.*, 2026, **8**, 2283

Metal–organic framework (MOF)-embedded magnetic polysaccharide hydrogel beads for rapid and selective adsorption of malachite green and crystal violet

Anni Fang,[a] Jie Gao,[a] Yunzhu Lu,[a] Lidong Wu[b] and Lei Cheng*[a]

This study aims to tackle water pollution caused by toxic triphenylmethane dyes—specifically malachite green (MG) and crystal violet (CV)—by developing a metal–organic framework (MOF)-based magnetic hydrogel microsphere (MMOF) using sodium alginate as the matrix. Magnetic MOF particles were embedded into the sodium alginate hydrogel to form porous, stable magnetic microsphere adsorbents. Scanning electron microscopy confirmed their morphology and structural features, showing abundant active sites and well-defined adsorption channels. Under the optimized conditions, the adsorption rate of MMOF for MG reached 97.67%, and the adsorption equilibrium time was 50 minutes. The adsorption rate of MMOF for CV was 97.33%, and the adsorption equilibrium time was 60 minutes, with maximum adsorption capacities of 1008.6 mg g^{-1} and 1100.1 mg g^{-1}, respectively, demonstrating outstanding dye removal ability. These magnetic microspheres also enabled rapid solid–liquid separation under an external magnetic field, supporting convenient operation and reusability. Overall, these composite microspheres represent a promising adsorbent for efficient removal of organic dye contaminants from aquatic product matrices, with strong potential for food safety applications.

Received 6th January 2026
Accepted 20th February 2026

DOI: 10.1039/d6na00008h

rsc.li/nanoscale-advances

1. Introduction

The discharge of dye-containing industrial wastewater is a major source of aquatic environmental pollution.[1] Due to the complex composition of synthetic dyes, their poor biodegradability, and the typically high pH and turbidity levels of dye effluents, effective treatment remains challenging.[2–4] Among these pollutants, malachite green (MG) and crystal violet (CV) – representative triphenyl methane dyes – can accumulate in aquatic organisms and metabolize into persistent derivatives such as latent malachite green (LMG) and latent crystal violet (LCV).[5–8] These metabolites increase overall toxicity and heighten human exposure risks through the food chain. In environmental and biological samples, these dyes typically exist at trace levels and coexist with complex matrices, posing significant challenges to the accuracy and reliability of analytical detection methods.[9–12] Therefore, developing rapid detection technologies with high sensitivity, strong selectivity, and good field applicability is essential for effective food safety monitoring.

Adsorption has become a mainstream technology for treating dye pollution in aquatic products due to its high efficiency and environmental compatibility.[13] As three-dimensional hydrophilic polymers, hydrogels offer strong adsorption potential because of their porous structures and high water-retention capacity.[14] However, conventional hydrogels often exhibit limited adsorption efficiency and poor selectivity toward organic dyes.[15] To overcome these limitations, recent research has focused on incorporating nanoparticles into hydrogel matrices to create hybrid materials with synergistically enhanced adsorption performance,[13,15,16] offering new avenues for efficient and eco-friendly treatment of dye wastewater. Alginate, a natural anionic polysaccharide derived from brown algae, forms stable three-dimensional hydrogels through ionic cross-linking with divalent or trivalent cations.[17] Functionalized alginate gels, characterized by low synthesis cost, abundant raw materials, and environmental friendliness, are considered a promising platform for the removal of cationic dye pollutants.[18]

This study introduces a novel composite adsorbent for the efficient removal of MG and CV by integrating magnetic materials and metal–organic frameworks (MOFs) within a hydrogel matrix. The incorporation of magnetic components significantly enhances the material's magnetic responsiveness, enabling rapid post-adsorption separation while improving recyclability, portability, and reusability. The spherical hydrogel

[a]*Key Laboratory of Plant Protein Innovation and Resource Development, China National Light Industry, Beijing Engineering and Technology Research Center of Food Additives, Beijing Technology and Business University, Beijing 100048, China*
[b]*CAS Key Laboratory of Separation Science for Analytical Chemistry, Dalian Institute of Chemical Physics, Chinese Academy of Sciences, 457 Zhongshan Road, Dalian, Liaoning 116023, China*

structure confines magnetic particles to localized regions, maintaining structural stability and increasing oxidation resistance. Furthermore, embedding MOFs as flexible scaffolds within the magnetic hydrogel network effectively increases specific surface area and optimizes pore architecture, significantly boosting adsorption capacity and selectivity toward MG and CV dyes. The effects of MOF loading and adsorbent dosage on the dye removal efficiency are systematically evaluated. The magnetic MOF (MMOF) hydrogel demonstrates strong separation performance and structural flexibility, enabling successful *in situ* dye removal from aquatic tissue surfaces and highlighting its strong potential for practical applications.

2. Materials and methods

2.1. Materials

The following chemical reagents were used in this study: ferric chloride hexahydrate ($FeCl_3 \cdot 6H_2O$), ferric chloride tetrahydrate ($FeCl_2 \cdot 4H_2O$), *N*,*N*-dimethylformamide (DMF; 99.5%, analytical grade), ammonium hydroxide, ethanol (99.5%, analytical grade), sodium alginate (SA; molecular weight (Mw) = 216.1215 g mol^{-1}, 1% viscosity = 550 mPa s, β-D-mannuronic acid : α-L-glucuronic acid ratio = 1 : 1), trifluoroacetic acid (TFA), polyvinylpyrrolidone (PVP; Mw = 40 000), acrylamide (AM), tetra(4-carboxyphenyl)porphyrin (TCPP; 97%), ammonium persulfate (APS), *N*,*N*-methylenebisacrylamide (BIS), calcium chloride ($CaCl_2$), *N*,*N*,*N*′,*N*′-tetramethylethylenediamine (TEMED; analytical grade), sodium citrate, zirconium chloride, acetonitrile (analytical grade), methanol (analytical grade), ammonia solution (analytical grade), malachite green (MG), crystal violet (CV), sunset yellow, methyl blue, and methylene blue. All reagents were purchased from McLean Company (Beijing, China).

2.2. Instruments

The instruments used in this study included a vortex mixer VM-500 pro (JOANLAB, Huzhou, China), a magnetic stirrer with oil bath (Li Chen, Shanghai, China), an ultraviolet-visible (UV-Vis) spectrophotometer (Shimadzu UV-3600Plu, Kyoto, Japan), a centrifuge (Xiangyi, China), a pH meter, a scanning electron microscope (Thermo Fisher Quattro S, Eindhoven, Netherlands), and a nanoparticle size and zeta potential analyzer (Zetasizer Nano ZS90, Malvern, UK).

2.3. Synthesis

2.3.1. Synthesis of Fe_3O_4@MOF. Under nitrogen protection, ferric chloride hexahydrate and ferric chloride tetrahydrate were dissolved in a water–ethanol mixed solvent, followed by the addition of ammonia solution. After centrifugation, Fe_3O_4 nanoparticles with an average diameter of 95 nm were collected. PVP powder was then added to the Fe_3O_4 nanoparticles and mixed thoroughly. Subsequently, TCPP, zirconium chloride octahydrate ($ZrOCl_2 \cdot 8H_2O$), TFA, and Fe_3O_4@PVP were added sequentially. The mixture was heated in an oil bath and washed successively with DMF and acetonitrile to ultimately obtain the Fe_3O_4@PVP composite. The resulting MOF material (Fe_3O_4@PVP@MOF) exhibited an average particle size of approximately 1100 nm and was stored in chromatographic-grade methanol. A nanoparticle size analyzer and zeta potential analyzer were employed to measure the particle sizes of Fe_3O_4 and Fe_3O_4@PVP@MOF, respectively.

2.3.2. Synthesis of the MMOF hydrogel. Fe_3O_4@MOF-545 (5.3 mg mL^{-1}), 19% AM (0.49 mL mL^{-1}), 1.5% APS (12 μL mL^{-1}), and 2% BIS (53.8 μL mL^{-1}) were sequentially added to syringe A and mixed thoroughly. Subsequently, 4.2% SA solution (0.45 mL mL^{-1}) was introduced into syringe A. In parallel, 4.2% SA solution (0.45 mL mL^{-1}) was loaded into syringe B. The two syringes were connected using a needle connector, after which 20 μL TEMED was added. The mixed solution was then dispensed dropwise into a 5 mol L^{-1} $CaCl_2$ solution at a controlled rate of approximately one drop per second. Strict control of the addition rate is essential: overly rapid addition leads to microsphere agglomeration, while excessively slow addition may cause premature gelation within the syringe, hindering smooth addition to the $CaCl_2$ solution. After the entire solution was added, the suspension was magnetically stirred for 1 h to obtain the MMOF hydrogel microspheres. The volume ratio of all components prior to TEMED addition directly corresponded to their ratio in the final reaction system.

2.3.3. Synthesis of the pure hydrogel. Under constant concentrations and amounts of all components in the MMOF hydrogel, AM, APS, and BIS were added to syringe A, while SA was loaded into syringe B. Subsequently, 20 μL TEMED was introduced into the system. The mixture was then dispensed dropwise into a 5 mol L^{-1} anhydrous $CaCl_2$ solution to form hydrogel microspheres. Following gelation, the microspheres were magnetically stirred for 1 h, filtered, and dried.

2.3.4. Synthesis of the magnetic hydrogel. The preparation procedure for the magnetic hydrogel was identical to that of the pure hydrogel, except that 30 mg of Fe_3O_4 powder was added to the formulation prior to gelation.

2.4. Adsorption of MG and CV on MMOF hydrogel

To establish adsorption calibration curves for CV and MG dyes and to assess the reliability of the analytical method, 10 mg of each dye was dissolved in 100 mL of ultrapure water to prepare 100 mg L^{-1} stock solutions. Standard working solutions of CV (2, 4, 6, 8, 10 mg L^{-1}) and MG (1, 2, 3, 4, 5 mg L^{-1}) were obtained by serial dilution. Absorbance was measured at wavelengths of 590 nm and 616 nm for CV and MG, respectively. The absorbance values for CV standard solutions were 0.045, 0.092, 0.138, 0.186, and 0.234, yielding a calibration equation of $A = 0.0234C + 0.0012$ ($R^2 = 0.9987$). For MG, absorbance values of 0.032, 0.066, 0.097, 0.134, and 0.171 resulted in the regression equation: $A = 0.035C - 0.004$ ($R^2 = 0.999$). The relative standard deviations (RSDs) were 1.25% for CV and 1.47% for MG, indicating excellent precision and reliability of the analytical method.

2.5. MG and CV removal using MMOF hydrogels

MMOF hydrogels exhibit strong adhesion to tissue surfaces, enabling precise, rapid, and selective removal of MG and CV. By

optimizing parameters such as solvent concentration, adsorption time, pH, and material composition, the maximum adsorption efficiency for MG and CV can be achieved. In the adsorption experiment, 30 mg of MMOF hydrogel was added to 10 mL of a 15 mg L^{-1} MG (or CV) solution, and the concentration change was monitored using a UV-vis spectrophotometer. The decolorization rate was calculated as follows:

$$X = \frac{C_0 - C_1}{C_0} \times 100\% \quad (1)$$

where C_0 is the absorbance of the original solution, C_1 is the absorbance after adsorption, and X is the decolorization rate.

2.6. Experimental conditions

Under conditions where both MG and CV concentrations were maintained at 15 mg L^{-1} and the solution pH was adjusted to 8.0, the adsorption behavior of the MMOF hydrogel was systematically optimized. In these experiments, the SA concentration was fixed at 4.2% (w/v), and the mass ratio of magnetic MOFs to SA was maintained at 12 : 1. This study primarily examined the adsorption performance of the MMOF hydrogel toward MG and CV and the corresponding adsorption kinetics. For evaluating the selective adsorption performance of MMOF hydrogels toward MG and CV, the concentrations of the reference dyes (methyl blue, methylene blue, and sunset yellow) were also uniformly set at 15 mg L^{-1}, with the reaction system pH controlled at 8.0. The material composition and preparation conditions for the MMOF hydrogels used in this section were identical to those employed in the adsorption kinetics experiments, ensuring methodological consistency.

2.7. Data processing methods

The data analysis methods used in this study primarily included data organization and data visualization. Data organization involved the systematic processing of raw data through classification, sorting, and coding to enhance its structure and facilitate subsequent analysis. Data visualization was employed to intuitively display the distribution patterns and intrinsic characteristics of data using graphical tools. In this work, bar charts and line charts are mainly utilized to present experimental results and highlight key trends.

3. Results and discussion

3.1. Characterization of MMOF hydrogels

3.1.1. Morphological characterization. Scanning electron microscopy (SEM) analysis of MMOF hydrogels revealed clear morphological differences compared with magnetic hydrogels. As shown in Fig. 1A–C and H–J, the magnetic hydrogels exhibit a relatively dense three-dimensional network at the macroscale. In contrast, MMOF hydrogels display a more developed porous structure with higher pore connectivity. At the microscopic level, the MMOF hydrogel surface is uniformly covered with numerous nanosheets/nanoparticles, forming a rough composite interface indicative of successful MOF-545 crystal incorporation. By contrast, the magnetic hydrogel surface shows only the inherent wrinkles of the polymer matrix and sparsely distributed magnetic particles.

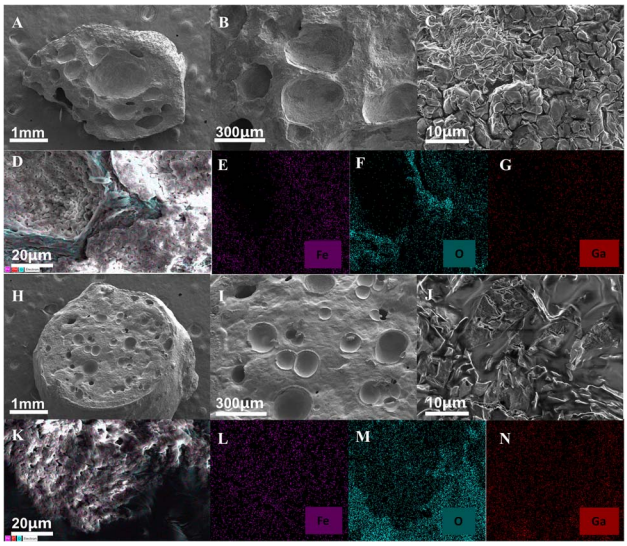

Fig. 1 Characterization of MMOF and magnetic hydrogels. (A–C) Scanning electron microscopy (SEM) images of MMOF hydrogels. (D–G) Energy dispersive X-ray spectroscopy (EDS) elemental mapping of MMOF hydrogels. (H–J) SEM images of magnetic hydrogels. (K–N) EDS elemental mapping of magnetic hydrogels.

The hierarchical pore architecture introduced by MOFs within the MMOF hydrogel, coupled with the significantly increased specific surface area, provides more accessible adsorption sites for dye molecules and enhances molecular diffusion and mass transfer efficiency. These microstructural features explain the superior adsorption capacity and kinetics of MMOF hydrogel compared to magnetic hydrogel. Energy-dispersive X-ray spectroscopy (EDS) was used for elemental mapping, and the results in Fig. 1D and E further confirm the successful incorporation of magnetic components, which impart strong magnetic responsiveness to the composite.

3.1.2. Pore structure analysis of MMOF hydrogels. Nitrogen adsorption–desorption analysis (Fig. 2A) shows that the MMOF hydrogels exhibit a typical type IV isotherm and H3-type hysteresis loop, confirming a hierarchical pore structure dominated by mesopores.[19] Quantitative measurements indicated a specific surface area of 40.6447 m^2 g^{-1} and a pore volume of 0.073 cm^3 g^{-1}. Further, density functional theory (DFT) modeling revealed an average pore diameter of 14.1274 nm.

The mesopore-dominated structure enhances adsorption through a dual mechanism: the large specific surface area and pore volume directly increase the number of accessible adsorption sites, supporting high adsorption capacity; simultaneously, the average pore diameter (14.1274 nm)—well matched to the kinetic dimensions of dye molecules, facilitates molecular diffusion and mass transfer within the pore channels and may improve adsorption selectivity toward target pollutants through spatial confinement effects.

The hysteresis loop obtained from vibrating sample magnetometry (VSM) analysis (Fig. 2C) indicates that both

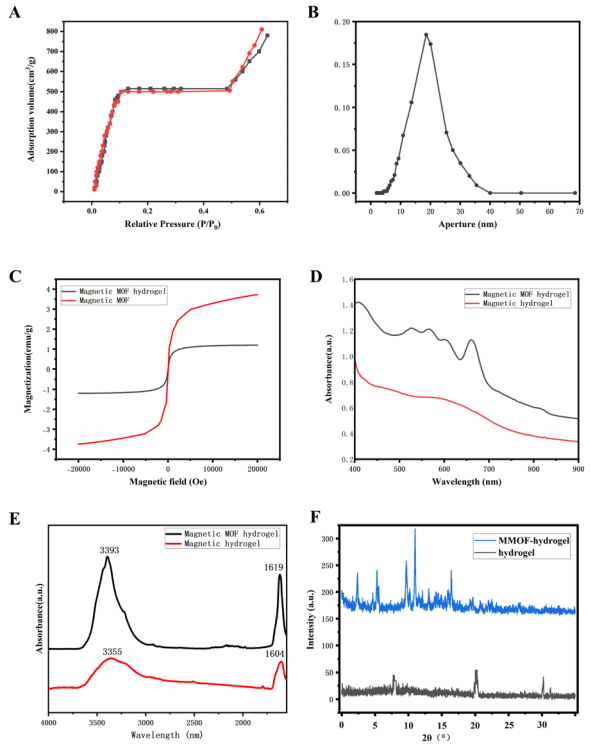

Fig. 2 Structural and adsorption characterization of the magnetic and MMOF hydrogels. (A) Adsorption isotherm of the magnetic and MMOF hydrogels. (B) Relationship between pore size and pore volume. (C) Nitrogen adsorption–desorption hysteresis curve. (D) UV-vis absorption spectrum of the magnetic and MMOF hydrogels. (E) Infrared spectra of Fe_3O_4 and MMOF hydrogels. (F) X-ray single crystal diffraction patterns of Hydrogel and MMOF hydrogel.

magnetic and MMOF hydrogels exhibit superparamagnetic behavior, with the magnetization curves passing through the origin and showing negligible hysteresis. The MMOF hydrogel exhibits a significantly lower saturation magnetization than the magnetic hydrogel, primarily due to the encapsulation and dilution effects of the non-magnetic hydrogel matrix on the magnetic nanoparticles. Despite this reduction, the composite maintains sufficient magnetic responsiveness for rapid separation under an external magnetic field.

The UV-vis absorption spectra (Fig. 2D) show broad and strong absorption behavior across 400–900 nm for both magnetic and MMOF hydrogels, with no characteristic distinct absorption peaks. Notably, the MMOF hydrogel exhibits significantly higher absorption intensity than the magnetic hydrogel across the entire wavelength range, particularly in the long-wavelength region. This enhancement suggests that the incorporated MOF not only introduces intrinsic light-absorbing properties but may also synergistically interact with magnetic components, thereby improving the composite's overall light-trapping efficiency.

Based on the clear identification of the material's elemental composition, to deeply analyze the chemical bonding mode and functional group structure of each element in the sample, this study further characterized the material using Fourier Transform Infrared Spectroscopy (FT-IR). As shown in Fig. 2E, by comparing the infrared spectra of the magnetic MOF hydrogel and the pure magnetic hydrogel, both showed characteristic absorption peaks at approximately 3393 cm^{-1} and 1619 cm^{-1}, which respectively belonged to the stretching vibration of hydroxyl/amino groups (O–H/N–H) in the system and the bending vibration of water molecules (or the asymmetric stretching vibration of carboxylate groups). Compared with the pure magnetic hydrogel, the magnetic MOF hydrogel exhibited significant blue shift and peak shape changes at these two peak positions, indicating that the introduction of the MOF structure enhanced the hydrogen bond interactions within the material and coordinated with the functional groups, such as carboxyl groups in the hydrogel network, thereby changing the vibration state of the relevant chemical bonds. This result confirmed that the MMOF and the hydrogel achieved an effective composite through chemical bonding, and there was a significant interaction between the components, which provided a crucial structural basis for the subsequent adsorption performance of the material.

The XRD comparison results in Fig. 2F provide conclusive evidence for the successful synthesis of the MMOF-545 composite hydrogel. A sharp and strong peak appears at $2\theta \approx 5°$ in the MMOF-545 complex, corresponding to the (100) crystal plane diffraction of MOF-545 (PCN-222), which is a fingerprint feature of its ordered mesoporous framework, confirming the successful introduction of the MOF phase. This peak is significantly broadened, indicating that the MOF exists in the form of nanocrystalline domains, which is conducive to exposing the active sites. Meanwhile, the overall scattering intensity of the composite material in the 15–30° range is significantly higher than the amorphous broad peak (~20°) of the pure hydrogel, which is due to the additional scattering of the organic ligands in the MOF. The results show that we have successfully integrated the crystalline, porous MMOF-545 into the amorphous flexible hydrogel network, constructing a composite system with high adsorption activity and good processability.

3.2. Optimization of adsorption conditions

3.2.1. Optimization of synthesis parameters. The adsorption performance of MMOF hydrogels is strongly influenced by the SA concentration and the volume of crosslinker used. As shown in Fig. 3A and B, the optimal adsorption of MG and CV occurs at a SA concentration of 4.2 wt% and a crosslinker volume of 3.0 mL, where the removal efficiencies exceed 95% for MG and 90% for CV. This ratio appears to generate a three-dimensional network structure that maximizes exposure of adsorption sites and facilitates efficient mass transfer. Increasing the SA concentration or crosslinker volume beyond this point leads to an overly dense gel structure, restricting dye molecule diffusion and reducing adsorption efficiency. Additionally, TFA volume optimization experiments (Fig. 3C) reveal that MMOF hydrogels prepared with 500 μL and 200 μL of TFA achieve the best adsorption performance for both dyes.

As shown in Fig. 3D, high adsorption efficiencies (>90%) for both MG and CV were achieved after an 8 h preparation process in a 90 °C oil bath. Fig. 3E and F further demonstrate that the

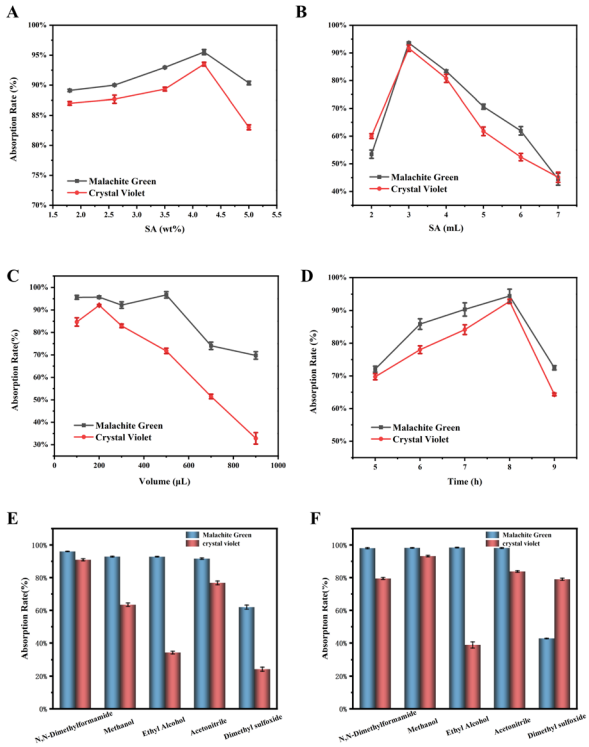

Fig. 3 Optimization of key synthesis parameters for MMOF hydrogel microspheres. (A) Effect of initial SA concentration on the adsorption performance. (B) Effect of SA dosage on the adsorption performance. (C) Effect of TFA dosage on the adsorption performance. (D) Effect of oil-bath reaction time on the adsorption performance. (E) Effect of different exchange solvents on the adsorption performance. (F) Effect of different eluents on the adsorption performance.

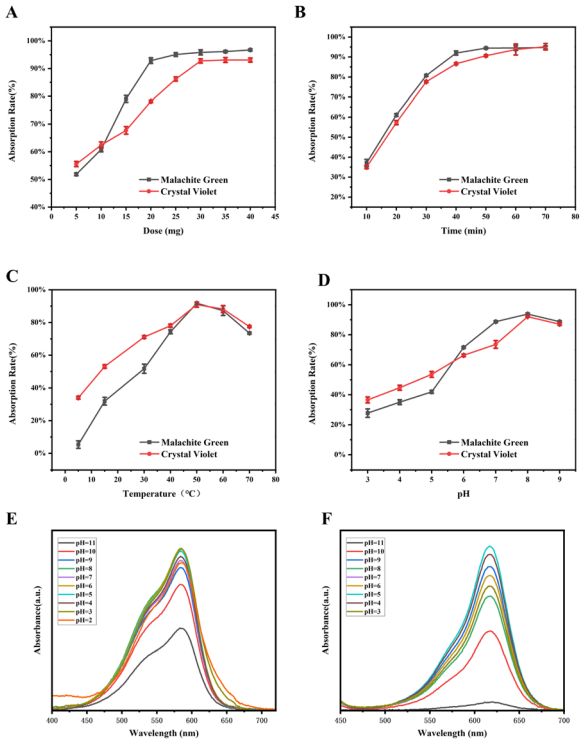

Fig. 4 Effects of operational parameters on dye decolorization and color stability. (A) Effect of MMOF hydrogel mass on adsorption rate. (B) Effect of adsorption time on adsorption rate. (C) Effect of temperature on adsorption rate. (D) Effect of pH on adsorption rate of CV and MG. (E) Effect of pH on CV color stability. (F) Effect of pH on MG color stability.

choice of organic solvents used during solvent exchange and washing significantly influences the final adsorption performance. Using DMF as the exchange solvent produced MMOF hydrogels with the highest adsorption capacities for both dyes, indicating that solvent polarity plays a critical role in regulating pore formation and surface chemistry. Additionally, washing the MMOFs with DMF and methanol yielded the best adsorption performance for MG and CV, respectively. These findings highlight the importance of optimizing synthesis parameters in tailoring material structure and achieving superior adsorption performance, providing evidence for the controlled synthesis of MMOF hydrogels.

3.2.2. Optimization of adsorption environment. In this section, by integrating adsorption kinetics, isotherm analysis, and pH-dependent behavior, the adsorption characteristics and mechanisms of MMOF hydrogels toward MG and CV are systematically elucidated. As shown in Fig. 4A, with the increase in adsorbent dosage, the adsorption rates of both dyes rapidly rises until saturation. Notably, MG reaches 90% removal at a lower dosage (25 mg), and across all tested conditions, its equilibrium adsorption capacity and adsorption rate are consistently higher than those of CV (30 mg). Kinetics studies indicate that MG achieves near-complete adsorption within 50 min, whereas CV requires 60 min to reach 90% of its maximum adsorption. As shown in Fig. 4C, temperature dependent experiments further reveal that the adsorption efficiencies for both dyes initially increase and then decrease within the 20–80 °C range, with optimal performance (>95%) at 50 °C. Overall, CV exhibits greater thermal stability than MG.

The UV-vis spectra in Fig. 4E and F show that both dyes remain structurally stable between pH 3–9, with no significant changes in peak positions or intensities, confirming that dye degradation does not interfere with adsorption measurements. The pH-dependent adsorption results (Fig. 4D) indicate that both MG and CV maintain high adsorption efficiencies under acidic to neutral conditions (pH 3–7), while adsorption rates decrease significantly under strongly alkaline conditions (pH > 8). The highest adsorption performance is observed at pH 8 (>95%). At this weakly alkaline condition, functional groups such as carboxyl groups within the MMOF hydrogel network are fully deprotonated, generating a high density of negative surface charges. These negatively charged sites strongly attract the cationic MG and CV molecules through electrostatic interactions, which serve as the dominant adsorption mechanism.[20] Additionally, this pH environment provides abundant stable adsorption sites for dye molecules, supporting high adsorption capacity.[21]

Selecting pH 8 rather than more alkaline conditions is essential for balancing adsorption efficiency with material

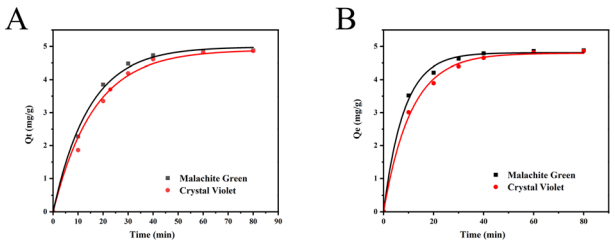

Fig. 5 Dynamic adsorption models for MMOF hydrogel microspheres. (A) Pseudo-first-order kinetic model. (B) Pseudo-second-order kinetic model.

stability. Although higher pH values may further increase the negative charge density on the surface, they can also induce MOF hydrolysis or metal node detachment, compromising pore structure, reducing adsorption performance, and potentially causing secondary pollution. Therefore, pH 8 provides near-optimal electrostatic adsorption while preserving the structural integrity and recyclability of the hydrogel's three-dimensional network, ensuring reliable performance in practical applications (Fig. 5).

3.3. Dynamic adsorption models

To further investigate the adsorption kinetics of MG and CV on MMOF hydrogel microspheres, pseudo-first-order and pseudo-second-order kinetic models were employed, as shown in Fig. 5. The corresponding fitting parameters are listed in Tables 1 and 2. The mathematical expressions for pseudo-first-order, pseudo-second-order, and intra-particle diffusion models are provided in eqn (2)–(4).[22–25]

$$\log(Q_e - Q_t) = \log(Q_e) - \frac{K_1}{2.303}t \quad (2)$$

$$\frac{1}{Q_t} = \frac{1}{K_2 {Q_e}^2} + \frac{1}{Q_e} \quad (3)$$

$$Q_t = K_3 t^{0.5} + C \quad (4)$$

where Q_e is the equilibrium adsorption capacity (mg g^{-1}); Q_t is the adsorption capacity at time t (mg g^{-1}); C denotes the boundary layer thickness; K_1 and K_2 are the rate constants for the pseudo-first-order and pseudo-second-order models, respectively; K_3 is the intra-particle diffusion rate parameter; and t represents time.[21,26–28]

Table 3 Parameters of the intra-particle diffusion model

	First stage			Second stage			Third stage		
	K_1	C_1	${R_1}^2$	K_2	C_2	${R_2}^2$	K_3	C_3	${R_3}^2$
MG	1.028	−0.580	0.998	0.366	2.285	0.992	0.024	4.677	0.970
CV	0.878	−0.500	0.997	0.424	1.580	0.994	0.058	4.378	0.991

As shown in Tables 1 and 2, the adsorption of MG and CV by MMOF hydrogel microspheres shows excellent agreement with both pseudo-first-order and pseudo-second-order kinetic models. The R^2 values for each model are greater than 0.9, indicating that both models reliably describe the adsorption behavior of the MMOF hydrogels. Additionally, the equilibrium adsorption capacities calculated from both models closely match the experimentally measured values, further confirming the accuracy and reliability of the kinetic analysis.

However, given that pseudo-second-order models generally describe chemisorption-dominated processes and provided slightly better fitting results, the pseudo-second-order model was considered more representative of the adsorption mechanism in this system. This hydrogel demonstrated outstanding adsorption performance for both dyes, with a notably higher adsorption rate constant for MG than for CV, indicating stronger chemical affinity or lower mass transfer resistance toward MG. Despite these kinetic differences, the material ultimately reached similar saturated adsorption capacities for both dyes, demonstrating its broad application potential as an efficient adsorbent for dye detection in aquatic products.

To further elucidate the rate-limiting steps during adsorption, the intra-particle diffusion kinetic model was applied. As summarized in Table 3, the adsorption process can be divided into three consecutive stages: an initial rapid membrane diffusion stage (confirmed by the negative intercept), a slower intra-particle diffusion stage that serves as the primary rate-limiting step, and a final equilibrium stage. The non-zero intercept ($C \neq 0$) of the fitted curve indicates that the adsorption process is jointly governed by membrane diffusion and intra-particle diffusion. The diffusion rate constants follow the

Table 1 Pseudo-first-order kinetic model parameters

	Q_e experimental (mg g^{-1})	K_1 (min^{-1})	Q_e calculated (mg g^{-1})	R^2
MG	4.878	0.100	4.876	0.999
CV	4.862	0.075	4.865	0.999

Table 2 Pseudo-second-order kinetic model parameters

	Q_e experimental (mg g^{-1})	K_2 (min^{-1})	Q_e calculated (mg g^{-1})	R^2
MG	4.876	0.0139	4.874	0.999
CV	4.864	0.0111	4.862	0.998

order: $K_1 > K_2 > K_3$, demonstrating that the adsorption process progresses from rapid surface adsorption to slower intra-pore diffusion before reaching equilibrium, with the intra-particle diffusion step exerting the dominant kinetic control.[29]

3.4. Analysis of the adsorption mechanism of MMOF hydrogel

The adsorption process at the solution–solid interface usually involves multiple mechanisms. This study proposes that the adsorption of target dyes by MMOF hydrogels may involve the following three main mechanisms.

The first is ion exchange adsorption. This mechanism stems from the substitution reaction between the exchangeable ions on the adsorbent surface and the oppositely charged ions in the target substance. In the MMOF hydrogel system, the cations such as H^+ on the material surface can exchange with the anions (such as Cl^- in cobalt blue) or cationic dyes (such as CV^+ in crystal violet) in the dye, thereby achieving a firm and efficient binding of dye molecules to the material surface through electrostatic interactions.

The second is electrostatic adsorption. Previous experimental results show that the surface charge property of MMOF hydrogels changes significantly with the pH value of the solution, and its adsorption performance for anionic dyes changes regularly. This phenomenon confirms that the electrostatic interaction between the material and the dye molecules is one of the key factors affecting the adsorption behavior.

The last is physical adsorption based on the porous structure. The synthesized MMOF hydrogels have a three-dimensional network structure composed of sodium alginate and polyacrylamide. Nitrogen adsorption–desorption tests show that it has a typical IV-type isotherm and H3-type hysteresis loop, indicating that the material has a developed mesoporous structure. Quantitative calculation shows that the specific surface area of this material is 40.6447 $m^2\ g^{-1}$, the pore volume is 0.073 $cm^3\ g^{-1}$, and the average pore diameter is 14.1274 nm. This high specific surface area, suitable pore size, and rich pore structure provide a large number of accessible adsorption sites for dye molecules, thus laying the physical foundation for high adsorption capacity.

3.5. Selectivity, recyclability, and storage stability of MMOF hydrogels

To investigate the selective adsorption efficiency of MMOF hydrogel microspheres toward MG and CV, five dyes were tested: methyl blue, CV, methylene blue, carmine red, and MG. The results in Fig. 6A show that the microspheres exhibit significantly higher adsorption capacity for MG and CV compared with the other dyes, indicating a degree of selectivity toward these specific dyes.

Due to the complexity of the food matrix, when selecting the magnetic solid-phase extraction agent, the influence of other interfering substances on the magnetic solid-phase extraction needs to be taken into consideration. By adding known concentrations of interfering components to the simulated system, the adsorption performance of the composite material

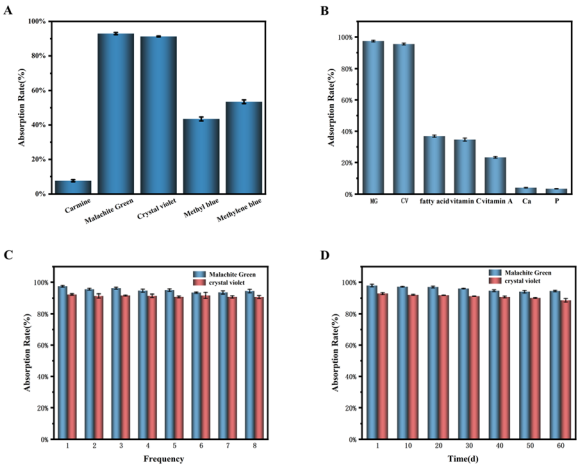

Fig. 6 Adsorption performance, selectivity, recyclability, and stability of MMOF hydrogel microspheres. (A) Adsorption rates of MMOF hydrogel microspheres toward different dyes. (B) Effect of coexisting components on MG and CV removal efficiency. (C) Effect of repeated recycling on MG and CV removal efficiency. (D) Effect of storage time on the adsorption performance of MMOF hydrogel microspheres.

for the target substance was investigated, as shown in Fig. 6B. In the solvent, in addition to the target pigment, common compounds (fatty acids, vitamin C, vitamin A, and metal ions) found in dairy products or beverages were added as interfering substances. The results showed that the synthesized material had little effect on the adsorption rate of the target pigments, carmine and lemon yellow, and the presence of coexisting components did not affect the detection effect of the target substances.

Excellent regenerability and storage stability are essential properties for advanced composite adsorbents. As shown in Fig. 6C, after eight consecutive adsorption–desorption cycles, the elution efficiency of the microspheres remained above 90%, demonstrating strong repeatability while supporting green and cost effective operational requirements. To further assess long-term stability, the MMOF hydrogel microspheres were dried at 60 °C, sealed, and stored for 60 days. Every 10 days, 300 mg of microspheres were tested in 10 mL of solvent for adsorption. As shown in Fig. 6D, adsorption efficiency rate remained consistently above 90% throughout the storage period, confirming the material's robust long-term stability.

Nitrogen adsorption–desorption analysis indicated that the MMOF hydrogel exhibits a typical type IV isotherm with an H3-type hysteresis loop, indicating a hierarchical pore structure dominated by mesopores. Quantitative analysis revealed a specific surface area of 40.6447 $m^2\ g^{-1}$ and a pore volume of 0.073 $cm^3\ g^{-1}$. Further, DFT modeling demonstrated an average pore diameter of 14.1274 nm. These structural parameters indicate the material has a high specific surface area and suitable pore structure, capable of providing abundant and accessible adsorption sites for MG and CV.[30] The mesoporous architecture enhances adsorption through a dual mechanism: the large specific surface area and pore volume increase the number of effective adsorption sites, while the pore diameter, well matched to the kinetic dimensions of dye molecules,

facilitates diffusion and mass transfer within the channels and may improve adsorption selectivity toward target pollutants through spatial confinement effects. Together, these features make the MMOF hydrogel's pore structure a key contributor to its high adsorption efficiency and separation performance.

4. Conclusions

In this study, we synthesized a magnetic MOF composite hydrogel (MMOF hydrogel) that demonstrated excellent performance for the adsorption and magnetic separation of MG and CV. This material enabled the targeted encapsulation of magnetic particles, greatly enhancing the magnetic responsiveness of the adsorbent. The MOF, integrated as a structural scaffold within the hydrogel's three-dimensional network, not only reinforced the material's mechanical stability but also improved its adsorption efficiency toward MG and CV. This hierarchical mesoporous structure facilitated rapid and controllable magnetic separation even in complex environmental matrices. The controllable magnetic separation technology enabled by MMOF hydrogels shows strong potential for automated operation, positioning the material as an efficient, environmentally friendly, high-throughput pretreatment platform for applications in aquatic product processing and broader environmental remediation contexts.

Author contributions

Anni Fang: writing – original draft, review & editing, investigation, formal analysis, conceptualization, resources, methodology original draft. Jie Gao: formal analysis. Yunzhu Lu: formal analysis. Lidong Wu: investigation. Lei Cheng: writing – review & editing, project administration, conceptualization, methodology, funding acquisition, supervision.

Conflicts of interest

There are no conflicts to declare.

Data availability

All data regarding this manuscript are already shown in the graphs of the main paper.

Acknowledgements

This work was supported by the National Natural Science Foundation of China (32372299).

Notes and references

1 X. Yan, Y. Q. Xia, C. P. Ti, J. Shan, Y. H. Wu and X. Y. Yan, *Sci. Total Environ.*, 2024, **914**, 12.
2 Q. Zhou, *Bull. Environ. Contam. Toxicol.*, 2001, **66**, 784–793.
3 M. Ismail, K. Akhtar, M. I. Khan, T. Kamal, M. A. Khan, A. M. Asiri, J. Seo and S. B. Khan, *Curr. Pharm. Design*, 2019, **25**, 3645–3663.
4 M. D. Lord, G. Neve, M. Keating and J. Budhathoki-Uprety, *ACS Appl. Polym. Mater.*, 2022, **4**, 6192–6201.
5 H. W. Sun and H. J. Qi, *Anal. Methods*, 2013, **5**, 267–272.
6 R. Z. Zhang, K. X. Liu, F. R. Jia, T. C. Xu and Y. J. Yang, *Anal. Methods*, 2025, **17**, 450–459.
7 M. H. G. Berntssen, R. Hannisdal, L. Buttle, R. Hoogenveen, M. Mengelers, B. G. H. Bokkers and M. J. Zeilmaker, *Food Addit. Contam. Part A-Chem.*, 2018, **35**, 1484–1496.
8 J. Eich, D. A. Bohm, D. Holzkamp and J. Mankertz, *Food Addit. Contam. Part A-Chem.*, 2020, **37**, 84–93.
9 G. Dowling, P. P. J. Mulder, C. Duffy, L. Regan and M. R. Smyth, *Anal. Chim. Acta*, 2007, **586**, 411–419.
10 M. Kaplan, E. O. Olgun and O. Karaoglu, *J. Chromatogr. A*, 2014, **1349**, 37–43.
11 Z. G. Zhang, B. Shi, L. P. Chen, L. Y. Lin and Y. Zhou, *Chin. J. Anal. Chem.*, 2006, **34**, 663–667.
12 J. Ascari, S. Dracz, F. A. Santos, J. A. Lima, M. H. G. Diniz and E. A. Vargas, *Food Addit. Contam. Part A-Chem.*, 2012, **29**, 602–608.
13 K. B. Tan, M. Vakili, B. A. Hord, P. E. Poh, A. Z. Abdullah and B. Salamatinia, *Sep. Purif. Technol.*, 2015, **150**, 229–242.
14 M. Gao, M. M. Sun, J. T. Bi, S. Z. Wang, X. F. Guo, F. Li, J. Liu and Y. Y. Zhao, *J. Water Process. Eng.*, 2025, **71**, 13.
15 V. V. Tran, D. Park and Y. C. Lee, *Environ. Sci. Pollut. Res.*, 2018, **25**, 24569–24599.
16 M. Z. Han, Z. H. Wang, Z. Y. Xie, M. X. Hou and Z. P. Gao, *Int. J. Biol. Macromol.*, 2025, **297**, 12.
17 H. Zhang, A. M. Omer, Z. H. Hu, L. Y. Yang, C. Ji and X. K. Ouyang, *Int. J. Biol. Macromol.*, 2019, **135**, 490–500.
18 H. Mittal, A. Al Alili, P. P. Morajkar and S. M. Alhassan, *J. Mol. Liq.*, 2021, **323**, 15.
19 A. Hojjati-Najafabadi, P. N. Esfahani, F. Davar, T. M. Aminabhavi and Y. Vasseghian, *Chem. Eng. J.*, 2023, **471**, 12.
20 N. S. Al-Kadhi, E. A. Abdelrahman, F. S. Alamro, F. A. Saad and D. S. Al-Raimi, *J. Inorg. Organomet. Polym. Mater.*, 2025, **35**, 5092–5104.
21 L. Huang, Z. F. Ning, Q. Wang, R. R. Qi, Y. Zeng, H. B. Qin, H. T. Ye and W. T. Zhang, *Fuel*, 2018, **211**, 159–172.
22 H. Long, H. F. Lin, M. Yan, Y. Bai, X. Tong, X. G. Kong and S. G. Li, *Fuel*, 2021, **292**, 9.
23 K. L. Tan and B. H. Hameed, *J. Taiwan Inst. Chem. Eng.*, 2017, **74**, 25–48.
24 B. Bai, D. Y. Rao, T. Chang and Z. G. Guo, *J. Hydrol.*, 2019, **578**, 10.
25 Z. Zhao, P. Li, Y. X. Guo, W. Wang, G. X. Fan and D. G. Teng, *ACS Sustain. Chem. Eng.*, 2025, **13**, 2141–2153.
26 W. X. Zhang, W. Z. Liang and Z. Zhang, *J. Membr. Sci.*, 2022, **663**, 9.
27 C. Y. Yuan, J. H. Ma, Y. D. Zou, G. S. Li, H. L. Xu, V. V. Sysoev, X. W. Cheng and Y. H. Deng, *Adv. Sci.*, 2022, **9**, 35.
28 Z. Q. Liu, G. Zhou, S. L. Li, C. M. Wang, R. L. Liu and W. J. Jiang, *Fuel*, 2020, **279**, 11.
29 P. L. Homagai, R. Poudel, S. Poudel and A. Bhattarai, *Heliyon*, 2022, **8**, 35–43.
30 M. Yousefian and Z. Rafiee, *Carbohydr. Polym.*, 2020, **228**, 9.